Title
Mineralized Peyronie's plaque has a phenotypic resemblance to bone.

Authors
Ustriyana, Putu
Hennefarth, Matthew R
Srirangapatanam, Sudarshan
et al.

Publication Date
2022-03-01

DOI
10.1016/j.actbio.2021.11.025

Peer reviewed

Acta Biomaterialia 140 (2022) 457–466

Contents lists available at ScienceDirect

Acta Biomaterialia

journal homepage: www.elsevier.com/locate/actbio

Full length article

Mineralized Peyronie's plaque has a phenotypic resemblance to bone

Putu Ustriyana[a,1], Matthew R. Hennefarth[a,1], Sudarshan Srirangapatanam[a], Haeyoon Jung[a], Yongmei Wang[a], Ling Chen[a], Tom F. Lue[b], Guiting Lin[b], Misun Kang[a], Marshall L. Stoller[b], Sunita P. Ho[a,b,*]

[a] Division of Preclinical Education, Biomaterials & Engineering, Department of Preventive and Restorative Dental Sciences, School of Dentistry, University of California San Francisco, CA, United States
[b] Department of Urology, School of Medicine, University of California, San Francisco, California, United States

ARTICLE INFO

Article history:
Received 14 September 2021
Revised 14 November 2021
Accepted 17 November 2021
Available online 21 November 2021

Keywords:
Biomineralization
Peyronie's
Heterotopic ossification
Bone

ABSTRACT

Mineralized Peyronie's plaque (MPP) impairs penile function. The association, colocalization, and dynamic interplay between organic and inorganic constituents can provide insights into biomineralization of Peyronie's plaque. Human MPPs ($n = 11$) were surgically excised, and the organic and inorganic constituents were spatially mapped using multiple high-resolution imaging techniques. Multiscale image analyses resulted in spatial colocalization of elements within a highly porous material with heterogenous composition, lamellae, and osteocytic lacuna-like features with a morphological resemblance to bone. The lower (520 ± 179 mg/cc) and higher (1024 ± 155 mg/cc) mineral density regions were associated with higher (11%) and lower (7%) porosities in MPP. Energy dispersive X-ray and micro-X-ray fluorescent spectroscopic maps in the higher mineral density regions of MPP revealed higher counts of calcium (Ca) and phosphorus (P), and a Ca/P ratio of 1.48 ± 0.06 similar to bone. More importantly, higher counts of zinc (Zn) were localized at the interface between softer (more organic to inorganic ratio) and harder (less organic to inorganic ratio) tissue regions of MPP and adjacent softer matrix, indicating the involvement of Zn-related proteins and/or pathways in the formation of MPP. In particular, dentin matrix protein-1 (DMP-1) was colocalized in a matrix rich in proteoglycans and collagen that contained osteocytic lacuna-like features. This combined materials science and biochemical with correlative microspectroscopic approach provided insights into the plausible cellular and biochemical pathways that incite mineralization of an existing fibrous Peyronie's plaque.

Statement of significance

Aberrant human penile mineralization is known as mineralized Peyronie's plaque (MPP) and often results in a loss of form and function. This study focuses on investigating the spatial association of matrix proteins and elemental composition of MPP by colocalizing calcium, phosphorus, and trace metal zinc with dentin matrix protein 1 (DMP-1), acidic proteoglycans, and fibrillar collagen along with the cellular components using high resolution correlative microspectroscopy techniques. Spatial maps provided insights into cellular and biochemical pathways that incite mineralization of fibrous Peyronie's plaque in humans.

1. Introduction

Aberrant human penile mineralization is known as mineralized Peyronie's plaque (MPP) [1]. The genesis of MPP is reliant on the formation of fibrotic plaque in the tunica albuginea of the penile corpora cavernosum [2,3]. Fibrillar proteins including collagen, elastin, and fibronectin were identified in the fibrotic plaque of the MPP [4,5]. MPP commonly forms on the dorsal aspect of the penis and can result in a loss of form and thereby function [6].

* Corresponding author at: Division of Preclinical Education, Biomaterials & Engineering, Department of Preventive and Restorative Dental Sciences, 513 Parnassus Avenue, Room HSW813, University of California, San Francisco, CA 94143-0758, United States
E-mail address: sunita.ho@ucsf.edu (S.P. Ho).
[1] Equal contribution and are first authors.

https://doi.org/10.1016/j.actbio.2021.11.025

The biomineralization process of PP [1] resembles heterotopic ossification (HO). HO results from fibroblast proliferation stimulated by repetitive mechanical insult to the tissue followed by microvascular injury and subsequent deposition of fibrin [7,8]. MPP results from differentiation of the fibroblasts in the tunica albuginea into myofibroblasts [9]. Myofibroblasts [10], smooth muscle cells [11,12], and pericytes [13,14] in blood vessels have been shown to undergo differentiation to osteogenic lineage *in vitro*. These cells are thought to be the initiators of biologically controlled biomineralization of the softer but inflamed matrices, subsequently culminating into an MPP. Surgical excision of MPP followed by mechanical therapy to restore penile form and function is the current clinical intervention [1]. Inflammation-related processes as well as the cation and anion recruitment including the metal ion Zn^{2+} are unknown. Various qualitative results focus on the ultrastructure of MPP [15–17]. Limited studies exist on the spatial-temporal localization of the biochemical and cytochemical markers of MPP and the surrounding soft tissue. Additionally, the spatial and chemical association of elements including calcium and phosphorus toward mineralization of collagen fibrils within the fibrotic plaque and the role of the neurovascular bundle in subsequent formation of MPP following an insult are yet to be understood. As such, some questions to ask include 1) does MPP grow from a mineralized nodule, and 2) does it begin as a fibrotic tissue and mineralize with phenotypic resemblance to bone? This study focuses on investigating the spatial association of matrix proteins and elemental composition of MPP by colocalizing Ca, P, and trace metal Zn with dentin matrix protein 1 (DMP-1), acidic proteoglycans, and fibrillar collagen along with the cellular components using high resolution correlative microspectroscopy techniques. Spatial maps of colocalized organic and inorganic constituents will provide insights into plausible biomineralization pathways of fibrotic Peyronie's plaque and help guide effective clinical interventions.

2. Materials and methods

2.1. Specimen preparation

MPPs ($n = 11$) were surgically excised from patients and these specimens were collected following a protocol approved by the UCSF Committee on Human Research Protection Program (IRB # 14–14,533). MPPs were fixed in 10% neutral buffered formalin at 4 °C (NBF, Richard-Allan Scientific, Kalamazoo, MI, USA) overnight, washed twice in phosphate buffered saline (PBS), and dehydrated in 50% ethanol/Milli-Q water solution at 4 °C.

2.2. Micro-X-ray computed tomography and data analyses

MPP specimens were scanned in 50% ethanol using a micro-X-ray computed tomography (micro-XCT) system (MicroXCT-200; Carl Zeiss Microscopy, Pleasanton, CA, USA) at 2× (9 µm/voxel), 4× (4.5 µm/voxel), 10× (1.8µm/voxel), and 20× (0.9 µm/voxel) magnifications with 1200 image projections, and an angle sweep from −93° to 93° Scanning of MPPs was performed with a 2 second exposure, source power of 40 W, and current of 200 µA.

2.2.1. Post-analysis of micro-XCT datasets

Mineral density (MD), porosity, and pore diameter of MPP were determined using 4× magnification scans. The reconstructed images of the specimens were analyzed using Avizo 2019.4 software (Fisher Scientific, Hillsboro, OR, USA). X-ray intensity values were converted from Hounsfield units to MD (mg/cc) following a published calibration protocol [18]. Higher and lower MD regions were labeled using a watershed algorithm [19]. The seeds for each region were based on mean ± standard deviation. Pores less than 100 µm in diameter were used to estimate pore density and network. Skeletonization function of the segmented pores was used to calculate the (minor) pore radius and network. Porosity of MPP was calculated by dividing the pore volume by the total volume. For high resolution analysis of pores, 20× magnification scans were used. Three regions of interests (ROIs) were taken from the specimen which corresponded to predominantly organic, mineralizing organic, and fully mineralized MPP. MD, pore diameter, and porosity were calculated for lower, middle, and higher mineralizing and mineralized regions.

2.3. Ultrastructural analyses

2.3.1. Scanning transmission electron microscopy and energy dispersive X-ray spectroscopy

MPPs ($n = 3$) were processed and embedded for ultrastructural examination using a scanning transmission electron microscopy (STEM) technique. Tissues were dehydrated gradually to 100% ethanol then infiltrated with LR-White resin (14,383; Electron Microscopy Sciences, Hatfield, PA, USA) in a gelatin capsule (70,110; Electron Microscopy Sciences) and polymerized for 2 days at 60 °C. Ninety nm thick sections were cut with an ultramicrotome (Reichert Ultracut E, Leica Microsystems, Inc., Buffalo Grove, IL, USA) and mounted on carbon/formvar coated Ni grids. Ultrathin STEM sections were examined under a field emission-scanning electron microscopy (FE-SEM) equipped with a STEM detector (Sigma VP500; Carl Zeiss Microscopy). The operation voltage was kept at 15 keV, aperture at 30 µm, and STEM images were collected.

Elemental maps and associated spectrum were acquired with an increased aperture of 60 µm with a 4 µm second dwell time using energy dispersive X-ray spectroscopy (EDX) detector (Bruker Nano Analytics, Billerica, MA, USA). The detector was calibrated using a copper standard and data were analyzed with Bruker Esprit software (version 2, Bruker). Quantification of EDX data was done using the standardless Cliff-Lorimer method and results are represented as percent atomic mass.

2.3.2. X-ray fluorescence microprobe spectroscopy and field emission scanning electron microscopy (FE-SEM)

The ultra-sectioned block surfaces were further scanned using X-ray fluorescence microprobe (micro-XRF) at beamline 10.3.2 of the Advanced Light Source (ALS) at Lawrence Berkeley National Laboratory (LBNL). All data was collected at 10 keV (for high atomic mass elements Ca and Zn) and Cak-50 eV (for low atomic mass elements including P) with a spot size of ∼20× 20 µm.

Following micro-XRF, the ultra-sectioned block surfaces were further examined under the FE-SEM using the field emission mode. The operation voltage was kept at 0.5 keV with the aperture at 30 µm as the subsequent images were collected. Regions with structural features were correlated with elemental spatial maps.

2.3.3. Colocalization and correlative image analyses of MD and elemental maps

For spatial correlation of MD and elemental (Ca, P, Zn) maps, tomograms displaying MD were translated, rotated, scaled, and cropped to register with corresponding elemental maps using Avizo. Registered MD and elemental maps were analyzed using Fiji software (developed at the National Institutes of Health, Bethesda, MD, USA, https://imagej.net/software/fiji/downloads) [20] for colocalization of elements and subsequent correlation of colocalized elements with mineral densities. Regions above mean counts of each element were segmented and overlaid on MD maps to colocalize elements within lower and higher MD regions. Spatial association between elements also was analyzed using correlative maps (code available on https://sunholab.ucsf.edu/codes) [21]. Further data analyses and visualization were performed in R version

3.6.3 (R Core Team 2020). 2D correlative scatter plots of MD-Ca, MD-P, and MD-Zn were obtained to identify the spatial association of different elements in lower and higher MD regions. Higher and lower MD regions were segmented using a threshold of mean counts. Binary masks corresponding to higher and lower MD regions were generated using Fiji software [20], and these masks were used to generate separate maps and histograms of Ca, P, and Zn corresponding to higher and lower MD regions (code available on https://sunholab.ucsf.edu/codes) [21].

2.4. Statistical analysis

Welch's independent *t*-tests were used to analyze the significance between MD of MPP and that of bones as reported in the literature [18,22,23]. All results were considered significant if $p < 0.05$ on a two-tailed significance test. Gaussian functions were generated to best fit the histograms. Results are reported as mean value ± standard deviation.

2.5. Histology

2.5.1. Staining for extracellular matrix, cells, collagen, proteoglycans, and other matrix proteins

MPP specimens were decalcified using 10% EDTA solution at 4 °C before being embedded in paraffin, and sliced into 4 µm sections. Sections were stained with H&E, alcian blue, Gomori trichrome, and Safranin-O following standard procedures.

2.5.2. Immunolocalization of DMP-1

DMP-1 was immunolocalized in MPP specimens using mouse anti-DMP-1 (Santa Cruz Biotechnology Inc., Dallas, TX, USA) (1:50) in paraffin-embedded sections and was detected with mouse-specific HRP/DAB detection IHC kit (ab42659, Abcam, Waltham, MA, USA) following the manufacture's instruction. The expression was visualized by diaminobenzidine (DAB) substrate and hematoxylin counterstaining.

3. Results

3.1. MD and pore diameter distribution within MPP

All MPP specimens ($n = 11$; representative in Fig. 1**A**) imaged using micro-XCT illustrated heterogeneous MD ranging from 901 to 1270 mg/cc with an average MD of 1036 ± 143 mg/cc (Fig. 1**B–1E**). Watershed algorithms localized two regions within each MPP specimen: lower and higher MD regions (Figs. 1**D** and 1**F**). The average MD value of MPP was comparable to that of physiologic cortical and alveolar bones, but was significantly higher than that of the physiologic trabecular bone (Fig. 1**G**).

Small radiolucent voids observed within MPP specimens illustrated pores (pore volume fraction) within the MPP. Pores less than the size of a one voxel were not included in porosity evaluation. Isolation and skeletonization of these small pores/voids yielded a 3D map of interconnecting network, of which the branches of the network were of various diameters and assumed a tortuous path (Figs. 2**A–2C**). The average pore diameter was 13 µm with the median porosity being 2.12 ± 0.69% (Fig. 2**C**). Larger pores within the MPP were consistently observed through plaque thickness; however, these were not analyzed. Analysis of pore diameter in the lower and higher MD regions showed that it was statistically lower relative to the pore diameter of the entire plaque ($p < 0.01$ for both) (Fig. 2**C**). Porosity in the lower and higher MD regions also was significantly lower (significantly less porous) than that in the entire plaque ($p < 0.01$). Furthermore, lower MD regions were significantly more porous than higher MD regions within MPP (Fig. 2**C**).

Each MPP specimen contained a varying degree of mineralization. Three ROIs contained within different MD zones within the MPP specimen were analyzed at 20X magnification, ROI 1 is within the predominantly organic region with an average pore diameter of 8.08 µm, MD of 520 ± 179 mg/cc, and porosity of 30%. ROI 2 illustrated the mineralizing region and ROI 3 the mineralized region with average pore diameters of 4.58 (11% porosity) and 3.86 µm (7% porosity) and MD of 673 ± 133 mg/cc and 1024 ± 155 mg/cc, respectively (Fig. 2**D**). Overall, the pores within ROI 3 were less connected compared to ROI 1, and there was a shift towards smaller pore diameters and porosity as Peyronie's plaque mineralized (Fig. 2**D**).

3.2. Presence of various organic and inorganic elements within MPP and the surrounding soft tissue

Electron microscopy of the MPP specimen also revealed regions of higher and lower MD with varying degrees of porosities (Fig. 3). High-resolution imaging focused on the interface between higher and lower MD illustrated smaller non-mineralized pores filled with mineralized particles. A different section from the same specimen also was viewed under the FE-SEM (Fig. 4). High-resolution microscopy confirmed the presence of non-mineralized pores within the mineralized tissue (Fig. 3). Smaller pores, however, resembled the morphology of osteocyte lacunae. These osteocytic lacuna-like features were filled with inorganic mineral constituents. Microscopy at a higher magnification also revealed that the mineralization surrounding these cell-like structures was occurring within a collagenous matrix. Within the MPP specimen, the mineralized region was comprised of mainly Ca and P with an average Ca/P ratio of 1.48 ± 0.06 as determined by EDX (Fig. 5). Sodium (Na), magnesium (Mg), carbon (C), and nitrogen (N) were also present in the surrounding soft tissue.

3.3. Colocalization of different inorganic elements within MPP

Mineral density from micro-XCT and elemental maps of Ca, P, and Zn from micro-XRF of MPP specimen are shown in Figs. 6**A** and 6**B**. Elemental maps were segmented into higher and lower MD regions. Ca and P were colocalized within the higher MD region, while Zn was observed at the interface of higher and lower MD regions and in lower MD regions. These co-localizations were also confirmed in the histograms of Zn counts in different MD regions (Fig. 6**C**). The highest Zn peak was observed in the lower MD regions (Fig. 6**C**, black arrowhead and #).

3.4. Histological staining and immunolocalization of proteins in MPP

Micro-XCT of the paraffin block from which sections were cut to immunolocalize DMP-1 revealed X-ray opaque regions (Fig. 7**A**). H&E staining of decalcified MPP revealed the X-ray opaque region as eosin rich-matrix with cells (Fig. 7**B**, red dashed outline). Gomori trichrome stain of the section revealed collagen in the X-ray opaque regions (Fig. 7**C**, red dashed outline). However, the X-ray opaque regions were not stained positive for alcian blue but were surrounded with alcian blue-positive matrix (Fig. 7**D**, red dashed outline). The X-ray opaque regions also were stained positive for Safranin-O (Fig. 7**E**, red dashed outline). The presence of blood vessels surrounded by fast green-positive staining were apparent within the outlined region. Within these mineralized regions, cells were identified inside the lacunae, and the matrix surrounding the lacunae was positive for DMP-1, suggesting osteocytic phenotype (Fig. 7**F**, red dashed outline).

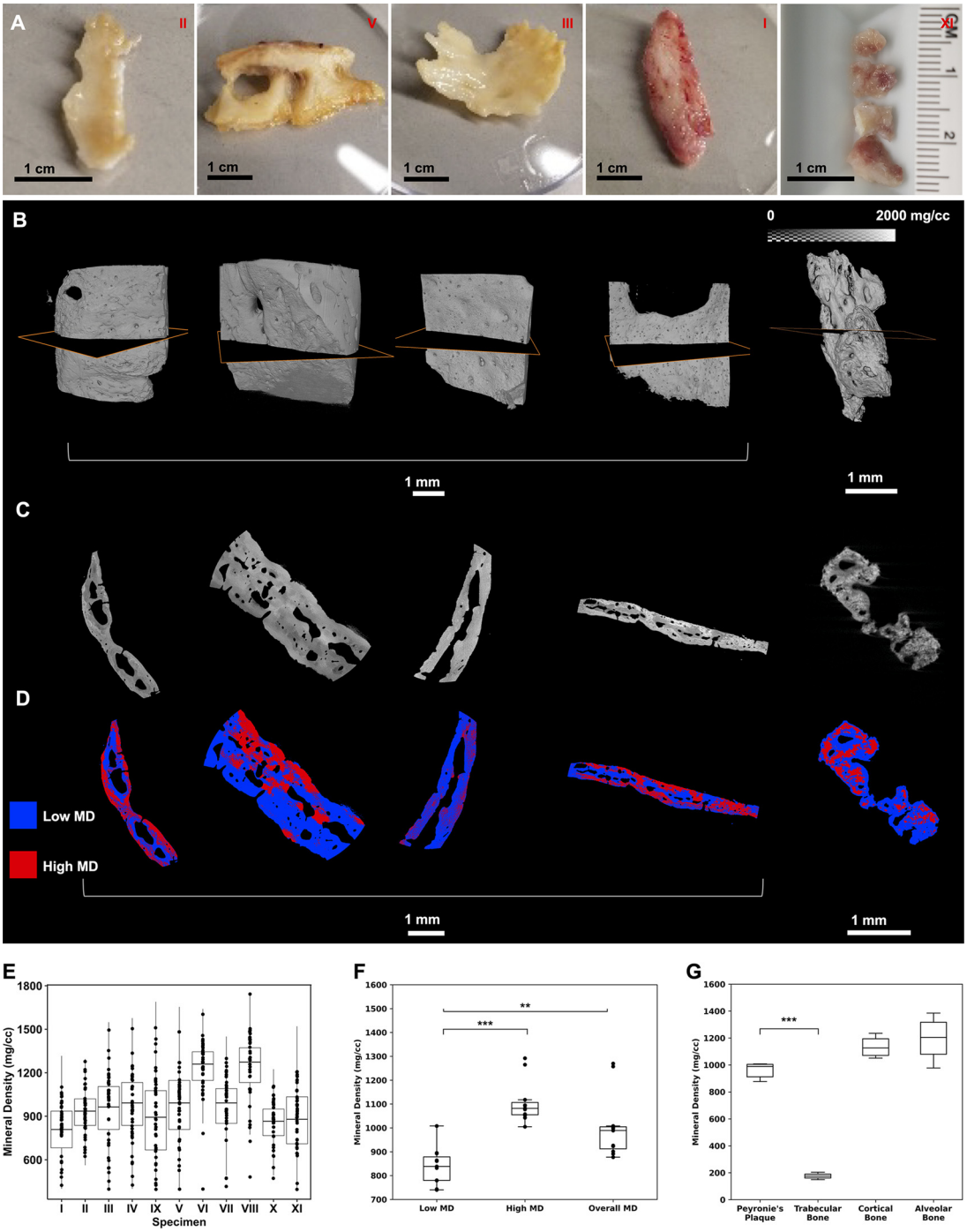

Fig. 1. Mineralized Peyronie's plaque (MPP) has different mineral densities. **(A)** Surgically removed MPPs from humans of different shapes and sizes are shown. **(B)** 3D rendered volumes of the plaques illustrate regions of distinct mineral densities. A location of 2D virtual section **(C)** outlined in orange is shown in the 3D volume of MPP. **(C, D)** Lower (blue) mineral density regions surround larger and smaller voids in contrast to higher mineral density regions (red). **(E)** Box plots illustrate variation in mineral densities within each specimen (I-XI). **(F)** An average of lower, higher, and overall mineral densities of MPP are compared with **(G)** average mineral densities of human skeletal trabecular [26], cortical [26], and alveolar bones [26]. A significant difference between MPP and trabecular bone ($p < 0.001$) was observed.

4. Discussion

Insights into penile biomineralization were gathered through an interdisciplinary approach of materials science and biology. Methodologies congruent with these perspectives have enabled us to co-localize trace metals/elements such as Zn in an organic matrix rich in acidic osteogenic proteins and polyanionic proteoglycans. The presence of Zn in MPP provides insights into two plausible mutually exclusive or inclusive 1) inflammatory and 2) enzymatic pathways involved in the mineralization of a fibrotic penile plaque.

The phenotypic features of MPP including the lamellae (**Supplemental Figure 1**) and osteocytic lacuna-like features resemble bone [24–26]. Higher MD regions of MPP were similar to human physiological cortical [27] and alveolar [27] bone ($p > 0.05$) and were statistically different from trabecular bone [27] ($p < 0.001$) (Fig. 1). The inorganic makeup of MPP, however, is chemically similar to that of bones regardless of their type. MPP is a porous ma-

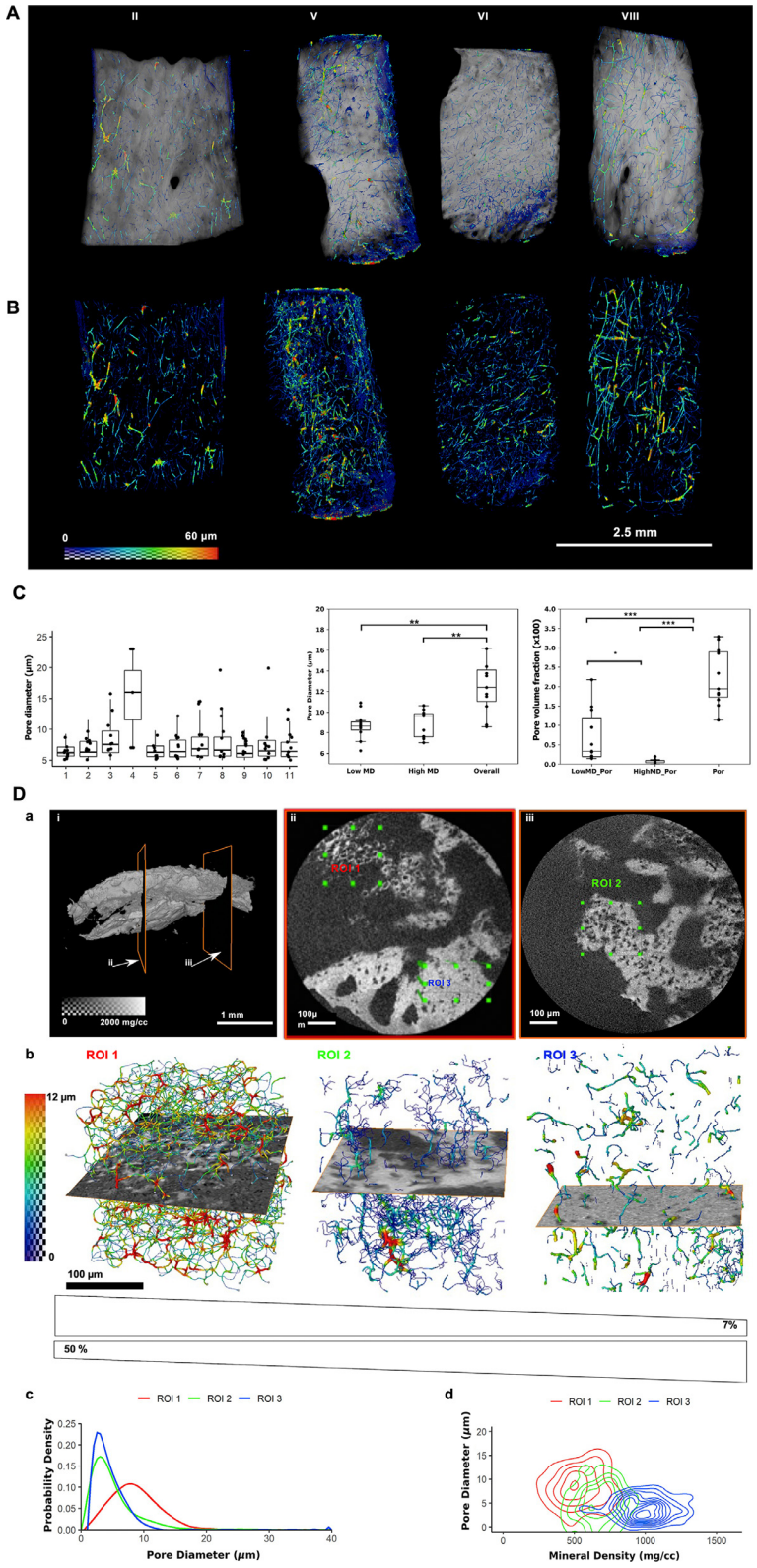

Fig. 2. Porosity of MPP decreases with increased mineral density, and MPP contains a tortuous network that changes with degree of mineralization. (A) Spatial maps of porous networks illustrate pore diameters up to 60 µm. (B) 3D rendered volumes of MPPs illustrate varying morphology and distribution of smaller diameter pores. (C) Box plots illustrate pore diameter and pore volume fractions for lower and higher mineral density regions, and the excised plaque. Significant differences between groups are indicated with *: $p < 0.05$, **: $p < 0.01$, and ***: $p < 0.001$. (D) 3D rendered volume and X-ray tomograms of MPP illustrate lower to higher mineral density regions of interest (ROI 1–3, green boxes). 2D virtual slices show the location of ROIs 1 (red), 2 (green), and 3 (blue) within the MPP (a). The tortuous network identified in ROI 1 disappeared with increasing mineral density. Regions of lower mineral density contained higher pore percentage, and degree of porosity decreased with increasing degree of mineralization (b). Distribution of the pore diameter with spline fit within each region (c) and an overlap of correlated data between pore diameter and mineral density for the three regions are shown (d).

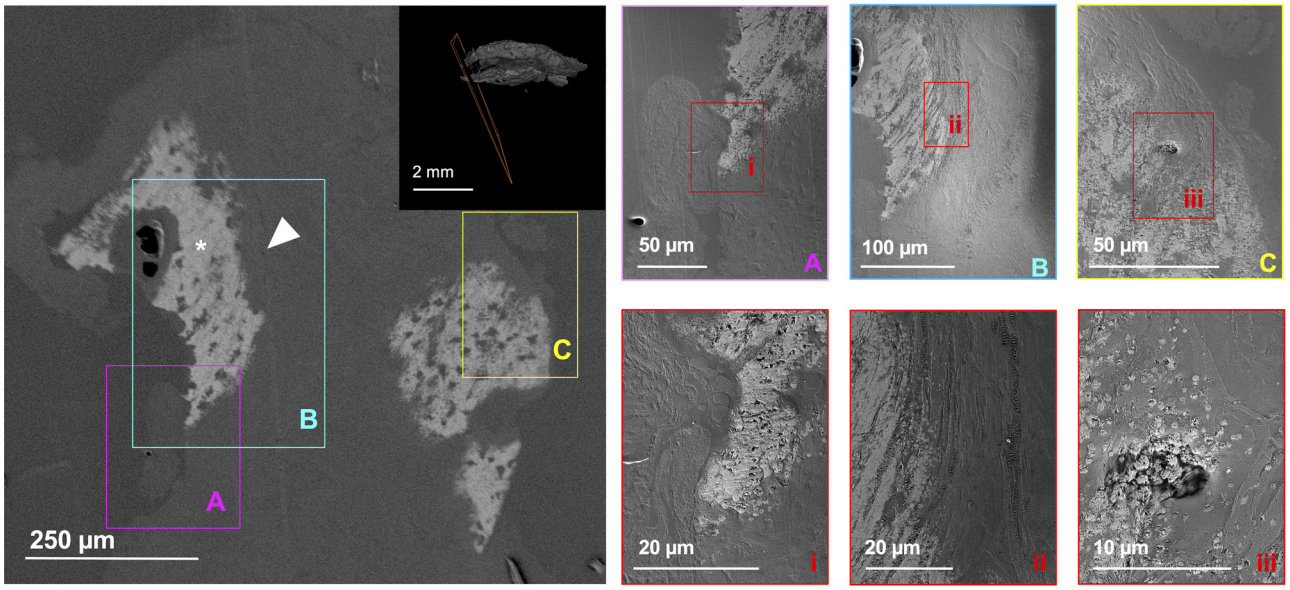

Fig. 3. Representative structures of lower and higher mineral density regions in Peyronie's plaque reveal clusters of smaller but electron dense mineralized particles. (A-C) SEM images contain interfaces between higher (asterisk) and lower (arrowhead) mineral density regions of MMP. Red boxes (i-iii) represent the locations of higher-resolution images.

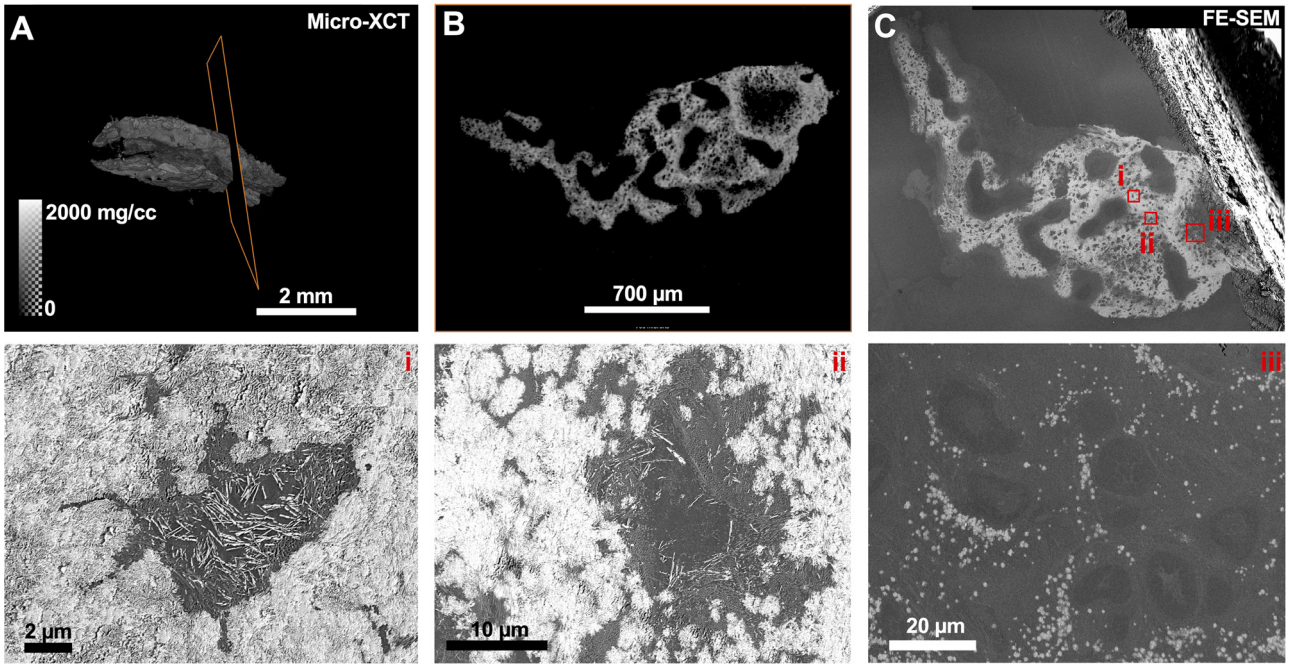

Fig. 4. MPP consists of regions with varying mineral densities and mineralized particles of different sizes. MPP **(A)** illustrates a representative 2D XCT tomogram **(B)** with inherent heterogeneity in mineral density and porosity **(C)**. Various "clusters of mineralized nodules" around cell bodies (i-iii, the locations can be seen in (C)) are shown.

terial wherein lower MD region with larger pores and morphological resemblance to vasculature (> 100 µm) and smaller pores (10 µm) in higher MD region 10–20 µm osteocytic lacuna-like features (Figs. 2–5) [28]. The smaller diameter pores of 10–20 µm osteocytic lacuna-like features observed in higher MD regions were confirmed by FE-SEM and STEM, and this size was well within the range observed using X-rays. The interconnected tortuous network between smaller diameter voids (lacunae) was plausibly representative of the canaliculi connecting these cells. The presence of these lacunae suggests their involvement in maintaining MPP albeit pathological.

The higher concentrations of Ca and P in the mineralized regions of MPP with a lower Ca/P ratio of 1.48 ± 0.06 (hydroxyapatite has a Ca/P ratio of 1.67 [29]) suggests a phase between tricalcium phosphate and calcium oxide [29]. The presence of sodium and magnesium, albeit trace amounts, further supports the resemblance of MPP with human skeletal bone [30,31]. The platelet-shaped minerals intertwined within and on type I collagen fibrils (Fig. 4**C** (i and ii), **Supplemental Figure 2**) are indicative of their intrafibrillar and extrafibrillar association with collagen [32,33]. Future studies on tissue sections using electron/X-ray diffraction

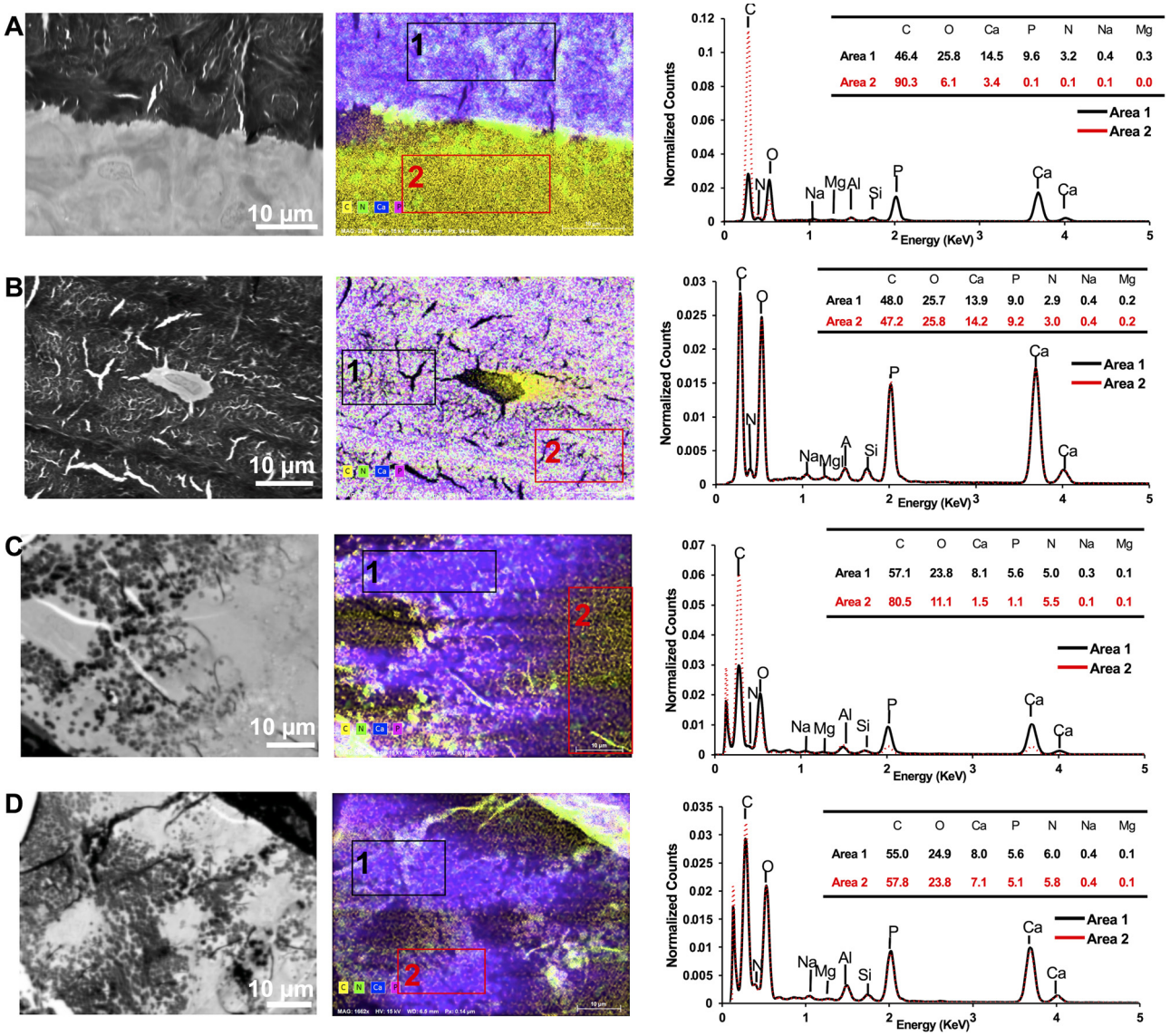

Fig. 5. Osteocytic lacuna-like regions were contained in higher mineralized regions with Ca and P as elemental composition, and in lower mineralized regions with carbon (C) and nitrogen (N) as the elemental composition. Regions (A-D) illustrate different osteocytic lacuna-like areas within the MPP. These areas consist of varying counts of different elements from predominant organic and inorganic regions.

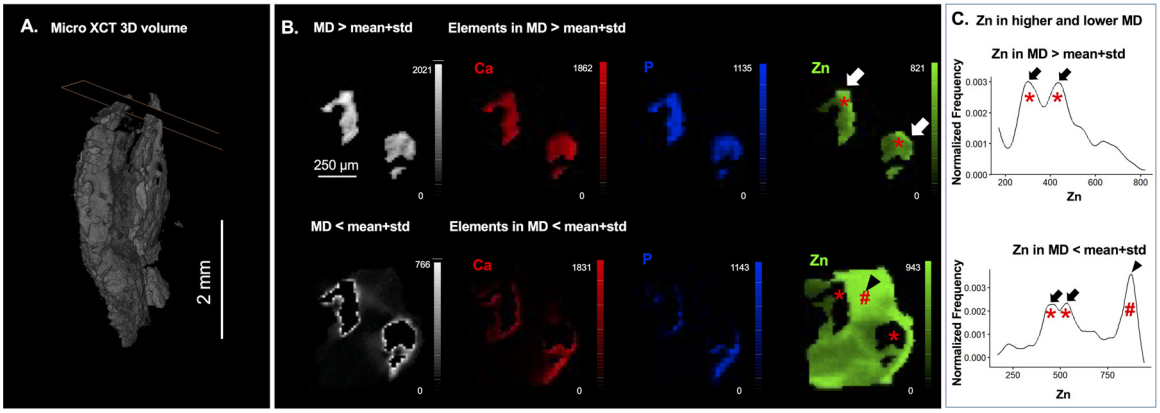

Fig. 6. Lower mineral density (MD) regions contain higher zinc (Zn) counts. (A) The location of the 2D virtual section is shown in the 3D-rendered volume. **(B)** Elemental maps from lower and higher MD regions are shown. **(C)** Histograms illustrate Zn counts in lower and higher MD regions. Arrowheads (#) and arrows (*) denote lower and higher MD regions, respectively, and are shown in spatial maps (B).

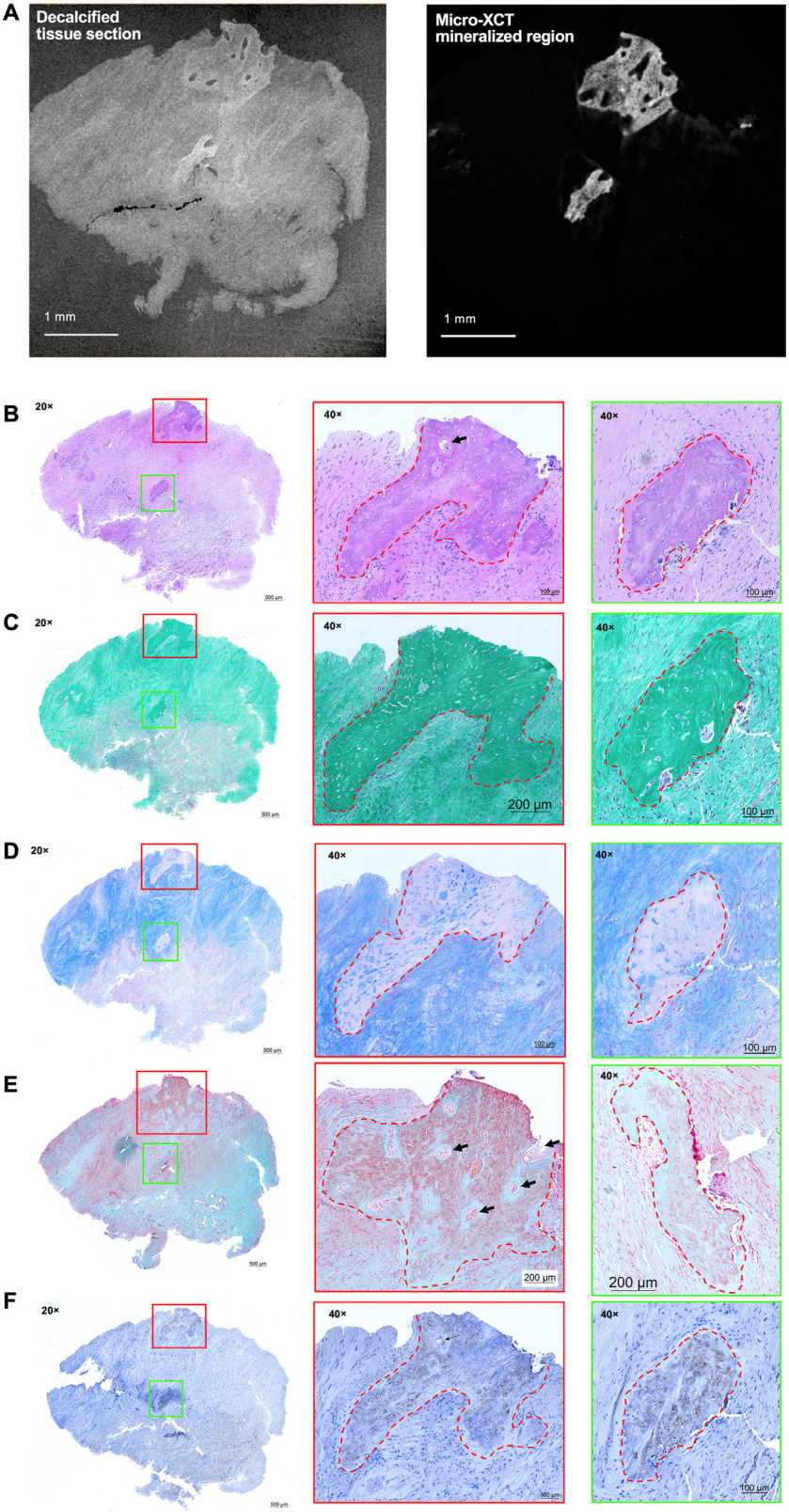

Fig. 7. Histology: Osteocytic lacuna-like regions were localized within higher mineralized collagenous and DMP-1-positive matrix that also is lower in Zn counts. However, this region is surrounded by a softer matrix with higher Zn counts. Presence of blood vessels within these regions also were observed. (A) 2D virtual section illustrates regions with higher mineral density. (B) H&E illustrates distribution of cells relative to the matrix, and plausibly nerves (black arrow). (C) Gomori trichrome staining illustrates collagenous matrix in both harder (outlined) and softer regions. (D) Alcian Blue staining reveals the absence of negatively charged proteoglycans in the higher mineralized regions (outlined). (E) Safranin-O counterstained with fast green illustrates the plausible presence of cartilaginous tissues within the higher mineralized regions (outlined). Fast green-positive areas surrounding blood vessels within the outlined regions with nerves were observed (black arrow). (F) DMP-1 was immunolocalized in higher mineral density regions (outlined), that also contained nerves (black arrows).

would reveal the type and phase of the mineral, that is, crystalline or amorphous.

Changes in the extracellular matrix (ECM) (Figs. 7**B** and 7**C**), particularly at the interface of two dissimilar biomaterials/tissues, the tunica albuginea and the corpora cavernosum, can create differential biomechanical strain, potentiate inflammatory cascades resulting from insults, and can trigger the differentiation of fibroblasts to myofibroblasts [34]. This process of inflammation and the initiation of fibroproliferation resembles the first of the four hallmark stages of HO [34]. The presence of Safranin-O hints at the presence of proteoglycans, which are present in higher concentrations in cartilaginous tissues (Fig. 7**E**), resembling the next stage of HO, which is chondrogenesis [34]. The maturation of the osteogenic matrix is marked by the immunolocalization of DMP-1 [34] in the perilacunar regions and higher MD regions of MPP (Fig. 7**F**). Taken together, it is likely that changes in tissue compliance including increased elastin production (data not shown) could alter this soft tissue-like phenotype to a harder tissue containing osteonal and lamellar features similar to bone. Despite this phenotypic resemblance to bone, the elucidation of whether a fibrotic Peyronie's plaque converts to an MPP through a fibrous vs. a fibrocartilaginous transformation is further warranted.

An exciting finding in this study is the presence of Zn. Zn was identified at the interface of soft and hard matrices and in adjacent harder bone-like tissue (Fig. 6). We contend that the presence of Zn is relatable to matrix metalloproteases (MMPs) in the softer and inflamed tissue surrounding MPP. MMPs are Zn-dependent endopeptidases that degenerate the ECM proteins including collagen [35,36]. This proteolysis can alter extracellular signaling which in turn can influence the gene expression and cell differentiation [37]. MMPs are involved in wound healing as well as bone or cartilage matrix degradation, remodeling, and repair [38,39]. The gene expressions of MMP-2 and MMP-9 were observed to be upregulated in Peyronie's plaque [40,41]. MMP-2 and MMP-9 also are expressed in healing wounds and are critical molecules during physiological formation of bone [42,43]. Therefore, during the MPP development and formation, a significant increase in local Zn expressions renders function of the MMPs and promotes collagen degradation. On the other hand, Zn also has been associated with NF-κB signaling pathway, one of the primary inflammatory pathways regulating genes related to **1)** apoptosis, adhesion, and cell proliferation (altered proliferation and apoptosis of fibroblasts are considered as the cause of abundant collagen production and accumulation in Peyronie's plaque); **2)** tissue remodeling; **3)** the innate and adaptive immune responses; as well as **4)** sterile and nonsterile inflammatory pathways [44]. Zn-regulated sterile inflammatory pathways specifically affect expressions of various proinflammatory cytokines, chemokines, acute phase proteins, adhesion molecules, and growth factors [44]; all of which plausibly condition the chemistry of the tissue and facilitate ion recruitment.

A common argument related to Zn specifically within the context of biominerals, bone, and teeth are its functional roles with tissue non-specific alkaline phosphatase (TNAP) and NF-κB. TNAP is a key enzyme for biomineralization and hydrolyzes organic pyrophosphate (PP_i) to inorganic phosphate (P_i) [45]. TNAP deficiency leads to bone hypomineralization [45]. The Zn-dependent NF-κB pathway also has been associated with osteoblast, osteoclast, and osteocyte biology [44]; all of which are needed to maintain functional health status of skeletal bone. Understanding the biochemical and molecular expressions related to Zn concentrations would help direct preventive and therapeutic approaches to mitigate pathologic mineralization not limited to penile tissues.

In summary, the correlative microspectroscopic approach on quantitative spatial mapping of MD, elements, and matrix alluded to MPP as HO. Both MPP and HO appear to share mechanobiological pathways, that is, mechanical trauma as a possible cue for soft tissue conversion into a hard tissue. Overall, results suggest a systematic well-orchestrated interplay between the metal ion Zn^{2+} and matrix proteins that incite mineralization of Peyronie's fibrotic plaque.

5. Conclusions

Zinc ligand complexes could be localized at the interface between softer and harder tissues of MPP, indicating the role of Zn-related biochemical pathways in the biomineralization of fibrotic Peyronie's plaque. Future studies should investigate the phase of mineralized particles, i.e., amorphous or crystalline, in association with the ECM proteins through the use of chemo- and mechano-biological functional assays. These mechanistic models will reveal the direct influence of shifts in cellular expressions and differentiation. These cellular processes result in a shift in tissue compliance; all of which are necessary to map the biomineralization pathways to mitigate heterotopic mineralization in tissues which otherwise would result in loss of function.

Funding

This research was funded by the Program in Biomineralization Studies (PiBiomS), Department of Urology, School of Medicine, UCSF. PiBiomS is a partnership between the Schools of Dentistry and Medicine at UCSF to investigate the cause of various pathologic biominerals in humans.

Declaration of Competing Interest

The authors declare no competing interests.

Acknowledgements

The authors thank Ms. Grace Nonomura for her help in specimen preparation. The authors additionally thank the Biomaterials and Bioengineering Correlative Microscopy Core (http://bbcmc.ucsf.edu), UCSF for the use of their MicroXCT-200 and SIGMA 500-VP Field Emission Electron Microscope – Scanning and Transmission. This research used beamline 10.3.2 of the Advanced Light Source, a Department of Energy Office of Science user facility under contract DE-AC02–05CH11231. The authors would like to acknowledge Dr. Sirine Fakra for her help and assistance at beamline 10.3.2.

Supplementary materials

Supplementary material associated with this article can be found, in the online version, at doi:10.1016/j.actbio.2021.11.025.

References

[1] J.F. Smith, T.J. Walsh, T.F. Lue, Peyronie's disease: a critical appraisal of current diagnosis and treatment, Int. J. Impot. Res. 20 (5) (2008) 445–459.
[2] D. Ralph, N. Gonzalez-Cadavid, V. Mirone, S. Perovic, M. Sohn, M. Usta, L. Levine, The management of Peyronie's disease: evidence-based 2010 guidelines, J. Sex Med. 7 (7) (2010) 2359–2374.
[3] B.H. Smith, Peyronie's disease, Am. J. Clin. Pathol. 45 (6) (1966) 670–678.
[4] F. Parhami, Y. Tintut, J.K. Patel, N. Mody, A. Hemmat, L.L. Demer, Regulation of vascular calcification in atherosclerosis, Z. Kardiol. 90 (Suppl 3) (2001) 27–30.
[5] N. Mody, Oxidative stress modulates osteoblastic differentiation of vascular and bone cells, Free Radical Biol. Med. 31 (4) (2001) 509–519.
[6] J.F. Smith, T.J. Walsh, S.L. Conti, P. Turek, T. Lue, Risk factors for emotional and relationship problems in Peyronie's disease, J. Sex Med. 5 (9) (2008) 2179–2184.
[7] C. Meyers, J. Lisiecki, S. Miller, A. Levin, L. Fayad, C. Ding, T. Sono, E. McCarthy, B. Levi, A.W. James, Heterotopic Ossification: a Comprehensive Review, JBMR Plus 3 (4) (2019) e10172.
[8] M. Jalkut, N. Gonzalez-Cadavid, J. Rajfer, Peyronie's Disease: a Review, Rev. Urol. 5 (3) (2003) 142–148.
[9] A.A. Hussein, A. Alwaal, T.F. Lue, All about Peyronie's disease, Asian J. Urol. 2 (2) (2015) 70–78.

[10] J. Hjortnaes, C. Goettsch, J.D. Hutcheson, G. Camci-Unal, L. Lax, K. Scherer, S. Body, F.J. Schoen, J. Kluin, A. Khademhosseini, E. Aikawa, Simulation of early calcific aortic valve disease in a 3D platform: a role for myofibroblast differentiation, J. Mol. Cell Cardiol. 94 (2016) 13–20.
[11] T. Liu, J. Lin, T. Ju, L. Chu, L. Zhang, Vascular smooth muscle cell differentiation to an osteogenic phenotype involves matrix metalloproteinase-2 modulation by homocysteine, Mol. Cell. Biochem. 406 (1–2) (2015) 139–149.
[12] S. Jono, M.D. McKee, C.E. Murry, A. Shioi, Y. Nishizawa, K. Mori, H. Morii, C.M. Giachelli, Phosphate regulation of vascular smooth muscle cell calcification, Circ. Res. 87 (7) (2000) E10–E17.
[13] M.J. Doherty, A.E. Canfield, Gene Expression during Vascular Pericyte Differentiation, Crit. Rev. Eukaryot. Gene Expr. 9 (1) (1999) 1–17.
[14] M.S. Davidoff, R. Middendorff, G. Enikolopov, D. Riethmacher, A.F. Holstein, D. Muller, Progenitor cells of the testosterone-producing Leydig cells revealed, J. Cell Biol. 167 (5) (2004) 935–944.
[15] J.S. Vande Berg, C.J. Devine, C.E. Horton, K.D. Somers, G.L. Wright, M.S. Leffell, D.M. Dawson, S.H. Gleischman, M.J. Rowe, Peyronie's Disease: an Electron Microscopic Study, J. Urol. 126 (3) (1981) 333–336.
[16] J.S.V. Berg, C.J. Devine, C.E. Horton, K.D. Somers, G.L. Wright, M.S. Leffell, D.M. Dawson, S.H. Gleischman, M.J. Rowe, Mechanisms of Calcification in Peyronie's Disease, J. Urol. 127 (1) (1982) 52–54.
[17] A. Mersdorf, P.C. Goldsmith, W. Diederichs, C.A. Padula, T.F. Lue, I.J. Fishman, E.A. Tanagho, Ultrastructural Changes in Impotent Penile Tissue: a Comparison of 65 Patients, J. Urol. 145 (4) (1991) 749–758.
[18] S.I. Djomehri, S. Candell, T. Case, A. Browning, G.W. Marshall, W. Yun, S.H. Lau, S. Webb, S.P. Ho, Mineral density volume gradients in normal and diseased human tissues, PLoS ONE 10 (4) (2015) e0121611.
[19] J.B.T.M. Roerdink, A. Meijster, The watershed transform: definitions, algorithms and parallelization strategies, Fundam. Inform. 41 (1,2) (2000) 187–228.
[20] J. Schindelin, I. Arganda-Carreras, E. Frise, V. Kaynig, M. Longair, T. Pietzsch, S. Preibisch, C. Rueden, S. Saalfeld, B. Schmid, J.Y. Tinevez, D.J. White, V. Hartenstein, K. Eliceiri, P. Tomancak, A. Cardona, Fiji: an open–source platform for biological-image analysis, Nat. Methods 9 (7) (2012) 676–682.
[21] R.M. Sulyanto, M. Kang, S. Srirangapatanam, M. Berger, F. Candamo, Y. Wang, J.R. Dickson, M.W. Ng, S.P. Ho, Biomineralization of Dental Tissues Treated with Silver Diamine Fluoride, J. Dent. Res. (2021) 220345211026838.
[22] H.E. Meema, S. Meema, Compact bone mineral density of the normal human radius, Acta Radiol. Oncol. Radiat. Phys. Biol. 17 (4) (1978) 342–352.
[23] H. Chirchir, Limited Trabecular Bone Density Heterogeneity in the Human Skeleton, Anat. Res. Int. 2016 (2016) 9295383.
[24] M.L. Eisenberg, J.F. Smith, A.W. Shindel, T.F. Lue, Tunica-sparing ossified Peyronie's plaque excision, BJU Int. 107 (4) (2011) 622–625.
[25] I.E. Yilmaz, Y. Barazani, B. Tareen, Penile ossification: a traumatic event or evolutionary throwback? Case report and review of the literature, Can. Urol. Assoc. J. 7 (1–2) (2013) E112–E114.
[26] K.A. Ostrowski, D.D. Dugi, J.C.Hedges 3rd, J.M. Barry, Bone saw for calcified Peyronie's disease plaques, Urology 86 (2) (2015) 415–416.
[27] S. Srirangapatanam, Y. Ellenikiotis, N. Foreman, A. Raymundo, O. Almaqhafi, M. Kang, H.S. Swana, M.L. Stoller, S.P. Ho, Shape factors of bones and teeth affect mineral density maps, in: the 99th General Session of the IADR, the 50th Meeting of the AADR and the 45th Meeting of the CADR virtual, Washington D.C., USA, 2021.
[28] C.I. Levene, Histology—A Text and Atlas, J. Clin. Pathol. 29 (1) (1976) 82 -82.
[29] L. Wang, G.H. Nancollas, Calcium orthophosphates: crystallization and dissolution, Chem. Rev. 108 (11) (2008) 4628–4669.
[30] R.P. Heaney, Sodium, Potassium, Phosphorus, and Magnesium, Nutr. Bone Health (2015) 379–393.
[31] B. Brodziak-Dopierala, J. Kwapulinski, K. Sobczyk, D. Wiechula, Distribution of magnesium, calcium, sodium and potassium in tissues of the hip joint, Magnes. Res. 26 (3) (2013) 125–131.
[32] E.E. Golub, Biomineralization and matrix vesicles in biology and pathology, Semin. Immunopathol. 33 (5) (2011) 409–417.
[33] X. Su, K. Sun, F.Z. Cui, W.J. Landis, Organization of apatite crystals in human woven bone, Bone 32 (2) (2003) 150–162.
[34] K. Shimono, K. Uchibe, T. Kuboki, M. Iwamoto, The pathophysiology of heterotopic ossification: current treatment considerations in dentistry, Japanese Dental Sci. Rev. 50 (1) (2014) 1–8.
[35] T. Sorsa, L. Tjaderhane, T. Salo, Matrix metalloproteinases (MMPs) in oral diseases, Oral Dis. 10 (6) (2004) 311–318.
[36] L. Ravanti, V.M. Kähäri, Matrix metalloproteinases in wound repair (review), Int. J. Mol. Med. (2000).
[37] D. Vernet, G. Nolazco, L. Cantini, T.R. Magee, A. Qian, J. Rajfer, N.F. Gonzalez-Cadavid, Evidence that osteogenic progenitor cells in the human tunica albuginea may originate from stem cells: implications for peyronie disease, Biol. Reprod. 73 (6) (2005) 1199–1210.
[38] V.J. Uitto, C.M. Overall, C. McCulloch, Proteolytic host cell enzymes in gingival crevice fluid, Periodontol 31 (2003) 77–104 2000.
[39] K.B.S. Paiva, J.M. Granjeiro, Matrix Metalloproteinases in Bone Resorption, Remodeling, and Repair, Prog. Mol. Biol. Transl. Sci. 148 (2017) 203–303.
[40] M.S. Watanabe, T.R. Theodoro, N.L. Coelho, A. Mendes, M.L.P. Leonel, A.M. Mader, H.B. Nader, S. Glina, M.A.S. Pinhal, Extracellular matrix alterations in the Peyronie's disease, J. Adv. Res. 8 (4) (2017) 455–461.
[41] A. Qian, R.A. Meals, J. Rajfer, N.F. Gonzalez-Cadavid, Comparison of gene expression profiles between Peyronie's disease and Dupuytren's contracture, Urology 64 (2) (2004) 399–404.
[42] T. Salo, M. Mäkelä, M. Kylmäniemi, H. Autio-Harmainen, H. Larjava, Expression of matrix metalloproteinase-2 and -9 during early human wound healing, Lab. Invest. 70 (2) (1994) 176–182.
[43] J.S. Nyman, C.C. Lynch, D.S. Perrien, S. Thiolloy, E.C. O'Quinn, C.A. Patil, X. Bi, G.M. Pharr, A. Mahadevan-Jansen, G.R. Mundy, Differential effects between the loss of MMP-2 and MMP-9 on structural and tissue-level properties of bone, J. Bone Miner. Res. 26 (6) (2011) 1252–1260.
[44] M. Jarosz, M. Olbert, G. Wyszogrodzka, K. Mlyniec, T. Librowski, Antioxidant and anti-inflammatory effects of zinc. Zinc-dependent NF-kappaB signaling, Inflammopharmacology 25 (1) (2017) 11–24.
[45] J.L. Millan, M.P. Whyte, Alkaline Phosphatase and Hypophosphatasia, Calcif. Tissue Int. 98 (4) (2016) 398–416.